Acta Astronautica 208 (2023) 130–141

Contents lists available at ScienceDirect

Acta Astronautica

journal homepage: www.elsevier.com/locate/actaastro

# Prediction and optimization of thrust performance from plasma diagnostics in the inductively coupled plasma of an RF ion thruster

Yueh-Heng Li [a,b,c,*], Yi-Chien Chen [b], Sheng-Wen Liu [a,c], Alim Rüstem Aslan [d]

[a] Department of Aeronautics and Astronautics, National Cheng Kung University, Tainan, 70101, Taiwan
[b] International Master Degree Program on Energy Engineering, National Cheng Kung University, Tainan, 70101, Taiwan
[c] International Doctoral Degree Program on Energy Engineering National Cheng Kung University, Tainan, 70101, Taiwan
[d] Faculty of Aeronautics and Astronautics, Istanbul Technical University, Maslak, 34469, Sarıyer/İstanbul, Turkey

ARTICLE INFO

*Keywords:*
Radio-frequency ion thruster
Inductively coupled plasma
Radio-frequency
Kriging model

ABSTRACT

Ion thrusters have acquired extensive applications in the space industry with their advantages of high efficiency, high specific impulse, and long lifetime. To operate a radio-frequency (RF) ion thruster successfully, a high-frequency current must be generated to facilitate the discharge of inductively coupled plasma. In this study, with support of trial and error, it is discovered that the thrust performance of an RF ion thruster depends on not only the RF power but also on other critical parameters, such as the propellant flow rate, ion grids voltages, and RF input power. A surrogate model, namely – the Kriging model, is employed to simplify the estimation and optimization of thrust performance. The thrust and specific impulse are selected to be the crucial metrics for used Kriging models for categorizing all types of propulsions. On the basis of Kriging model simulations, the designed RF ion thruster can achieve a thrust of 1.9 mN, a specific impulse of 1649.5 s, and a thrust efficiency of 48% under a propellant flow rate of 4 sccm, grids' voltage difference of 2500 V, and an RF input power of 40 W.

## 1. Introduction

Micro-propulsion systems have numerous applications in the modern space industry. Particularly with the newly suggested 5 year rule their importance is increased as a de-orbiting facilitator for nano-micro spacecraft. Studies on these systems have attempted to decrease their weight and volume and increase their efficiency. Currently, two main types of electric propulsion systems exist: Hall thrusters and ion thrusters. Hall thrusters such as the XR-5 (US) [1], the SPT-140 (Russia) [2], and the PPS-5000 (Europe) [3] and ion thrusters such as the XIPS-25 (US) [4] and the T-5 (UK) [5] are used for various applications on a variety of spacecraft including smallsats for station keeping, orbital transfer and positioning, attitude control, and deep-space exploration.

Ion thrusters have acquired extensive applications in the space industry with their advantages of high efficiency, high specific impulse, and long lifetime. There are various types of ion thrusters. A radio-frequency ion thruster (RIT) is an electric propulsion device that utilizes inductively coupled plasma (ICP) to generate plasma and an ion optical system to obtain ion beams (thrust). RITs exhibit electrodeless discharge, do not produce a magnetic field, produce a homogeneous beam, and have tunable parameters. Compared with Hall thrusters, RITs have a simpler structure and higher ductility and malleability, which facilitates the use of RITs in the position maintenance and orbital transfer of geostationary satellites. Germany was the first country to develop an RIT, and RIT-10 from the University of Gieβen enabled the Artemis satellite to achieve a suitable geostationary orbit [6]. Moreover, the University has developed RITs with diameters ranging from 25 to 350 mm for meeting different power demands [7]. To cover the thrust range from 50 to 500 μN, μNRIT-2.5 was developed and tested for further investigation. Furthermore, this university has adopted RIT-10 to conduct comparative experimental studies by using iodine and xenon as working fluids [8].

Countries such as the United Kingdom, Russia, the United States, and France have conducted research on RITs. The University of Southampton developed the Micro Differential Gridded radio-frequency Ion Thruster (MiDGIT) for complex space applications, such as drag compensation and formation flying [9]. The MiDGIT has two control modes: (1) a control mode involving operation under a high specific impulse and thrust level and (2) a control mode involving operation under a relatively low thrust level. In the first control mode, the thrust range is approximately 200–780 μN, and the specific impulse is approximately 400–1100 s. In the second control mode, the thrust range is approximately 1–125 μN, the thrust resolution can reach 4 μN, and the

---

* Corresponding author. Department of Aeronautics and Astronautics, National Cheng Kung Univ., Tainan, 70101, Taiwan.
*E-mail addresses:* yueheng@mail.ncku.edu.tw, yuehheng.li@gmail.com (Y.-H. Li).

https://doi.org/10.1016/j.actaastro.2023.03.038
Received 17 January 2023; Received in revised form 19 March 2023; Accepted 26 March 2023

## Nomenclature

$A_s$ = screen grid area [m$^2$]
c = propagation velocity of electromagnetic waves in vacuum [ = 3.00 × 10$^8$ m/s]
$e$ = elementary charge [ = 1.6 × 10$^{-19}$ C]
$I_{bit}$ = impulse bit [μNs]
$I_b$ = ion beam current [mA]
$I_{sp}$ = specific impulse [sec]
$i$ = current [A]
$k$ = Boltzmann constant [ = 1.38064852 × 10$^{-23}$ m$^2$ kg · s$^{-2}$ K$^{-1}$]
$l_e$ = effective length of the acceleration [m]
$m'$ = mass flow rate [sccm] (For Argon, 1 sccm = 2.973 × 10$^{-8}$ kg/s = 29.73 μg/s)
$M_i$ = ion mass [kg]
$\mu_0$ = magnetic permeability of free space [ = 4π × 10$^{-7}$ H/m]
$n_e$ = electron density [m$^{-3}$]
$n_i$ = ion density [m$^{-3}$]
$P$ = power [W]
$P_{abs}$ = absorbed power [W]
$P_{loss}$ = power loss [W]
$P_{RF}$ = RF input power [W]
$q$ = ion charge [C]
$T$ = thrust [mN]
$V$ = voltage [V]
$V_b$ = voltage difference between grids [V]
$v_i$ = exhaust velocity of ions [m/sec]
$\delta$ = skin depth [μm]
$\varepsilon_0$ = permittivity of free space [ = 8.85 × 10$^{-12}$ F m$^{-1}$]
$\sigma_p$ = plasma conductivity [A·m$^{-1}$·V$^{-1}$]
$\upsilon_m$ = elastic collision frequency [s$^{-1}$]
$\varphi_s$ = anode sheath potential [V]
$\omega$ = angular frequency [rad/sec]

*Acronyms*

AC = Alternative Current
BIT = Busek's radio frequency Ion Thruster
CCP = Capacitively Couple Plasma
DC = Direct Current
E-mode = Capacitively coupled Electrostatic mode
H-mode = Inductively coupled Electromagnetic mode
ICP = Inductively Coupled Plasma
IV curve = Current-Voltage curve
LHS = Latin hypercube sampling
MAI = Moscow Aeronautical Institute
MCS = Monte Carlo sampling
MHz = Mega Hertz
MiDGIT = Micro Differential Gridded radio-frequency Ion Thruster
MRIT = Miniature Radio-Frequency Ion Thruster
NASA = National Aeronautics and Space Administration
μNRIT = Micro Newton Radio frequency Ion Thruster
RF = Radio Frequency
RF-ICP = Radio Frequency - Inductively Coupled Plasma
RIT = Radio frequency Ion Thruster

specific impulse is only approximately 5–220 s. In 2010, the Moscow Aeronautical Institute (MAI) of Russia established an RIT laboratory, and in 2013, the MAI began to study low-power (300 W) RITs, whose thrust and specific impulse can reach 8 mN and 3500 s, respectively [10]. American company Busek focuses on the applications of CubeSat and is committed to research on low-power RITs. In 2015, Busek produced the BIT-3 prototype, which is the world's first RIT to use iodine [11]. The iodine working medium of BIT-3 has a thrust range of approximately 0.66–1.24 mN and a specific impulse of up to 2640 s. This thruster is planned to be used in the National Aeronautics and Space Administration's (NASA) two 6U CubeSat missions, namely Lunar IceCube and LunaH-Map, to enable them to reach their target orbits [12]. To reduce the failure risk of the Laser Interferometer Space Antenna mission, Busek designed a 1-cm-class micro-RIT (BIT-1) for achieving a thrust resolution of 0.1 μN in the thrust range of 30–150 μN and used a new type of plasma igniter [13]. In response to the demand for the miniaturization of thrust devices for microsatellites and nanosatellites, Pennsylvania State University developed a Miniature Radio-Frequency Ion Thruster (MRIT) [11]. When the discharge chamber is conical and argon is used as the working fluid, the thrust range and specific impulse of this system are 1.45–59.0 μN and 5480 s, respectively [14]. French company ThrustMe developed NPT30, which has two sizes (1 U and 1.5 U), and in this system, xenon and iodine can be used as working fluids [15].

Currently, researchers investigate RITs by using theoretical analysis, numerical simulation [16], and experimental research. Theoretical analysis and numerical simulation mainly involve the modeling of the discharge process and beam extraction mechanism [17]. The modeling of the discharge process involves the analysis of the steady-state discharge mechanism and the calculation of the radio-frequency (RF) power (to optimize the parameter design) [18]. The modeling of the beam extraction mechanism involves examining the influences of the grid parameters on the extracted current, and the thrust performance can be improved through grid optimization [19]. The experimental method involves conducting the power coupling test to obtain the thruster's ignition power [20]. Most relevant studies have used the experimental method to examine the thrust performance of RITs [21]. A ground test platform with specific operation modes must be constructed to determine the variation law of thrust performance. The development of a tangible test platform is such a money/time-consuming process, and the universality (for all kinds of thrusters) is poor; therefore, the thrust performance was numerically investigated before the actual manufacturing of the platform. Information on the thrust performance under different parameters has considerable academic and practical value.

Recent studies of the RF-ICP ion thrusters have been focused on building a more reliable and practical global model since 2012. For example, Pascal Chabert et al. [22] aimed at solving the four global variables (the plasma density, the electron temperature, the neutral gas density, and the neutral gas temperature) with their proposed global (volume-averaged) model for Xenon. Andreas Reeh et al. (2019) [23], on the other hand, took not only the spatial ionization/excitation but also the effects of local charge and the power losses into consideration. As for other propellants, Pascaline Grondein et al. (2016) [24] utilized Iodine due to the rarity and costliness of Xenon. Compared with Xenon, the thrust efficiency was marginally higher for Iodine in similar operating conditions. In the year 2022, a series of global models for Argon (for the first time) were developed by Bernardo Magaldi et al. [25], which used the same propellant as that in this study. Those global models in the previous studies had shed light on the interrelationship among the input parameters that facilitate the performance prediction of RITs.

Little research has been carried out on the correlation among thrust performance without creating global models based on each thruster's condition. Instead of relying on these massive calculations, this study established a surrogate Kriging model of thrust performance by analyzing the internal physical processes of RITs. The functional parameter design was conducted for a RIT by using a mathematical model and empirical formula from the literature. Parameters such as the propellant flow rate, grids' voltage difference, and RF input power were input to the developed Kriging model to obtain metrics such as the thrust, specific impulse, efficiency, and mass utilization rate. Other variable, for instance, the RF coil structure, was included in the latest published paper [26] but not considered in this study since our coil has difficulty keeping in shape. The choice of propellant flow rate is to subvert the inaccurate concept of its proportional relationship with the thrust, which was earlier proved by this study [27]. Research on the distribution of voltage differences between the screen/acceleration grids was also shown in the literature [28] to interpret the mechanism of ion optics system. Last but not least, the influence of RF input power was investigated through a series of experiments — the paradox of thrust performance versus manufacturing cost [29]. With these parameters, a reliable Kriging model was constructed and analyze their effect on the design.

## 2. Methodology

### 2.1. Category & mechanism of ion thrusters

Ion thrusters are electric propulsion systems in which the grid system generates an electrostatic field to accelerate ions; that is, the grid system realizes ion convergence and acceleration to produce thrust because of its potential difference. The grid system usually comprises two or three refractory (molybdenum or graphite) porous thin sheets (i.e., grids). Several voltages are applied to these grids, which have regularly arranged apertures, to create an electric field to converge, accelerate, and eject ions for thrust production.

Based on the selected plasma generation method, most commonly used ion thrusters can be categorized as electron bombardment (Kaufmann), RF, or microwave thrusters. Ion thrusters can also be classified on the basis of the adopted propellant, energy input level, and engine size (radial diameter). In all types of ion thrusters, effective and efficient methods must be used to ionize the propellant. In general, ion thrusters have a low energy consumption per unit ion, high ionic current, high propellant ionization efficiency, and long lifetime. An ion thruster can be functionally divided into the following main components (Fig. 1):

(a) Thruster (contains an ionization chamber, a hollow cathode, an ion optic system, and a neutralizer)
(b) Power control unit (or power processing unit)
(c) Propellant feeding system
(d) Digital control interface

The operation of ion thrusters is described as follows:

1. The main cathode ejects primary electrons to the discharge chamber filled with propellant gas (e.g., xenon or argon).
2. These electrons are accelerated by the electromagnetic force of the discharge chamber and become ionized or collide with the propellant gas.
3. The collision between the primary electrons and the propellant gas generates second electrons, which collide with the primary electrons and form the discharge plasma.
4. The electrons are absorbed by the discharge chamber's anode, whereas the ions converge and accelerate on the upstream grid surface under the plasma sheath's voltage.
5. The accelerated ions are ejected as a collimated beam and generate thrust.
6. To ensure the electric neutrality of the entire system, a neutralizer sends the same number of electrons to the beam ions.

### 2.2. Gas discharge and breakdown

Ionized gases contain electrons, ions, and neutral atoms or molecules. Gas discharge refers to the production of a conduction current by an ionized gas generated by an external electric field. On the basis of the discharge mechanism, gas discharge can be of four types: glow discharge, arc discharge, spark discharge, and corona discharge. To obtain a preliminary understanding of various forms of gas discharge, the characteristic current–voltage (IV) curves of gas discharge can be analyzed. The gas discharge current varies with the voltage between the electrodes (Fig. 2 & Table 1).

### 2.3. Capacitively Coupled Plasma vs. inductively coupled plasma

Three main methods of plasma generation are used in laboratory and industrial environments: the gas discharge, laser radiation ionization, and ray radiation methods. The plasma source commonly used in material surface treatment often produces RF discharge, microwave discharge, low-frequency discharge, or direct-current (DC) discharge. RF ion sources that produce gas discharge are widely used in chemical vapor deposition, material modification, etching, coating, and other

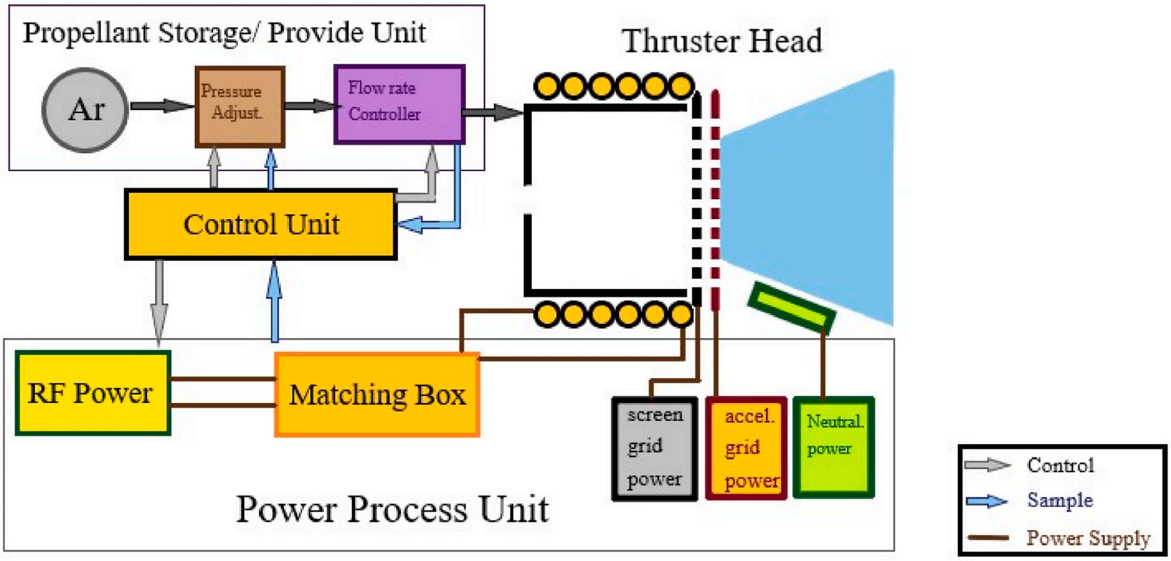

**Fig. 1.** Schematic of ion thruster mechanism.

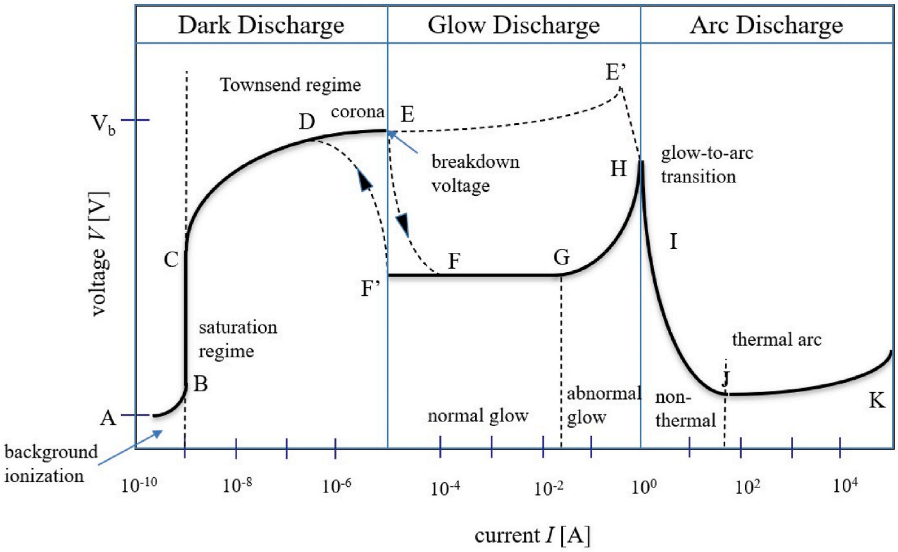

**Fig. 2.** IV curve of gas discharge regime.

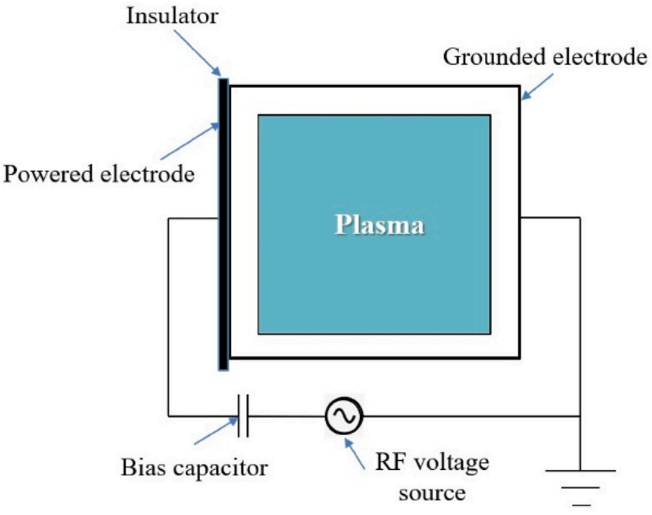

**Fig. 3.** Schematic of capacitively coupled plasma.

**Table 1**
Electric discharge regimes.

| Type | IV characteristic | Optical characteristic |
|---|---|---|
| *Townsend* | The discharge current is low. | The gap is filled with dim light, which tends to produce glow discharge. |
| *Glow* | The discharge is relatively steady. The discharge time is at the nanosecond level. | The luminous form is stable, and a bright glow occurs on the surface of the electrode. No continuous penetrating conductive channel is formed between the gaps. |
| *Spark* | The pulse width is at the level of several microseconds. A larger overshoot and longer recovery time occur after each discharge. | High-intensity luminescence appears instantaneously upon discharge, which is brighter than glow discharge. |
| *Surface flashover* | | Discharge channels develop mainly along the surface of the insulating struts. High-intensity luminescence appears on the surface of the insulating support during discharge. |
| *Arc* | The pulse width is of the order of several microseconds. The current peaks and voltage drop in arc discharge considerably exceed those in spark discharge and surface flashover. | The discharge causes the formation of an extremely bright through-conductive channel. When the supplied power is sufficient, the conductive channel can be maintained for a long time. |

applications [30]. Such plasma sources are usually driven by an alternating-current (AC) power source, with the frequency of AC power usually being 13.56 MHz. Compared with DC discharge, RF discharge results in more favorable conditions for plasma chemical reactions. In addition, the electrodeless discharge generated by the external electrode ensures the high purity, high efficiency, and low gas consumption of RF-ICP, which is convenient to use and can be applied in the surface treatment of insulators.

### 2.3.1. *Capacitively Coupled Plasma*

Capacitively coupled plasma (CCP) usually has a density of approximately $10^{15}$–$10^{16}\ \mathrm{m}^{-3}$. This plasma is generated between two parallel electrode plates by applying RF power to these plates (see Fig. 3). The primary discharge mode of CCP is capacitive discharge, which is also referred to as capacitively-coupled-mode (E-mode) discharge. The radius of the two plates used to generate CCP is generally 200 mm, and the distance between them is generally approximately 30–50 mm. The thickness of the plasma sheath is affected by changes in the plasma temperature and charged particle density. Charged particle loss from the plasma source mainly occurs on walls of the sheath, and a plasma sheath is formed irrespective of the type of discharge produced. When DC discharge is produced, the structure of the plasma sheath does not change with time, whereas when RF discharge is produced, the thickness of the plasma sheath increases and decreases with periodic changes in the excitation voltage. When the ion density is $n_i = 1 \times 10^{14}\ \mathrm{cm}^{-3}$, the thickness of the sheath is approximately $1.33 \times 10^{-5}$ cm.

### 2.3.2. *Inductively coupled plasma*

Inductively coupled plasma (ICP) usually has a density of $10^{16}$–$10^{18}\mathrm{m}^{-3}$. High-density plasma can reduce the ion bombardment energy to prevent physical damage of the discharge chamber and improve process selectivity. ICP is generated by passing an RF current through a coil or antenna, and a dielectric tube or window is typically used to isolate the generated ICP from the coil (see Fig. 4). ICP can be generated using a planar coil or cylindrical coil. The ICP produced using planar coils is often used to conduct reactions in large-scale production processing. This structure can enable large-area processing and can be used as plasma etching equipment. The anisotropic reaction in plasma etching usually requires the direction of incident ions to be perpendicular to the electrode direction, and this reaction is stronger at lower pressures. The ICP produced using cylindrical coils is often used in laboratory environments. It is small and flexible, does not require a specific chamber shape or the installation of air guides and other equipment outside the chamber, and does not pollute the electromagnetic environment in the chamber. This study investigated cylindrical RF-ICP. Unlike the discharge mode of CCP, the discharge mode of ICP includes two processes, namely E-mode and inductively-coupled-electromagnetic-mode (H-mode) discharge. The difference between the discharge modes of ICP and CCP lies in the heating mechanisms of these plasma types. Although CCP has the benefit of easier plasma ignition, ICP provides higher plasma densities (Experimental Characterization of the Capacitively Coupled RF-Plasma Thruster) [31]. Therefore, ICP is more widely used in surface processing and etching research than CCP. The basic principles of ICP are introduced in the following section.

## 2.4. Principle of RF-ICP

### 2.4.1. Fundamental of RF-ICP

Plasma generation occurs in the discharge chamber winding that contains an RF coil. The RF current generates an RF magnetic field through this coil. The inductive electric field $E$ is directed along the angular direction, whereas the generated inductive magnetic field $B$ is directed along the axial direction. Parameter $\delta$ denotes the skin depth. As the plasma density increases, the electric and magnetic fields decay exponentially. Moreover, the conducted energy is released in the skin depth and transferred to other areas of the discharge chamber [32]. Electrons are accelerated in the electromagnetic field, which increases their energy to the ionized potential of the introduced working gas. At this time, the neutral particles in the reactor are almost at room temperature, and a large quantity of electron energy is used to excite or ionize the working gas into plasma. In general, plasma is mainly composed of positive and negative ions, electrons, photons, excited atoms and molecules, ground-state atoms and molecules, and radical groups, while particles will break covalent bonds, transition electron layers or outer electron energy different factors such as level form different types of charged particles with different energy levels. The "steady-state" plasma density produced by ionization and recombination is usually a few percent of the density of the introduced neutral atoms and molecules [33]. Plasma is generated at the center of the discharge chamber, and the entire system is electrically neutral. The electron density $n_e$ is the same as the ion density $n_i$. During electron diffusion toward the discharge vessel's wall, the average velocity of electrons becomes considerably higher than that of ions because of the small mass reaching the wall first. Although some electrons recover or bounce off the wall, negative charge still accumulates on the wall. Because of their negative potential, the device wall repels electrons and attracts ions. Ions accumulate on the wall surface and reduce the number of electrons near the wall. When the electron current density reaching the wall is equal to the ion current density, the negative potential of the wall does not change. Finally, a sheath region that loses electrical neutrality is formed. In the capacitive coupling mode, electrons are mainly accelerated by the sheath layer. After entering the inductive coupling mode, the electron energy is mainly obtained from the skin depth. At this time, the sheath thickness of the generated RF-ICP is only a few Debye lengths, and skin depth $\delta$ is considerably larger than the Debye length. Usually, a high-frequency induction discharge arc is generated at the edge of the skin depth under the influence of the induced magnetic field, and the arc acquires an increasingly cylindrical shape under nonpolar discharge [34]. In the discharge process, a high coil current is required to maintain the plasma density; however, the power loss increases with the coil current. To obtain a high coupling efficiency, the wall of the discharge chamber must be sufficiently thin [27].

### 2.4.2. Skin depth

The generated RF-ICP typically oscillates in the gigahertz range; therefore, the electromagnetic field generated by the RF power source (frequency: 13.56 MHz) cannot easily penetrate this plasma [35]. Because of the limited length of the inductive coil, the magnetic field lines diverge at both ends of the coil. When the cold working gas is introduced into the system, the plasma density decreases radially outward, whereas the electromagnetic field increases radially outward and finally forms a skin depth. In this paper, the high-plasma-density area in the center of the discharge chamber is referred to as being "outside the skin depth," and the low-plasma-density area around the vessel wall is referred to as being "inside the skin depth." In the H mode, the skin depth is an essential means of RF-ICP coupling energy. The exponentially decaying electromagnetic field in the skin depth has a strong acceleration effect on electrons; thus, the electron density of RF-ICP can be abruptly changed during E mode–H mode transitions. increased mutagenicity. Therefore, the skin depth $\delta$ is an essential basis for designing the radius of RF-ICP. On the basis of the elastic collision frequency of the generated plasma, skin depth $\delta$ can be divided into non-collision and collision.

1. The non-collision skin depth of the plasma is:

$$\delta = \frac{c}{\omega_p} \tag{1}$$

($\upsilon_m \ll \omega$, that is, the elastic collision frequency is less than the electromagnetic wave frequency.) where c is the propagation velocity of electromagnetic waves in vacuum and $\omega_p$ is the oscillation frequency of the generated plasma. At an RF frequency of 13.56 MHz, the generated RF-ICP plasma density is $10^{16}$–$10^{17}\mathrm{m}^{-3}$, and the calculated $\delta$ range is approximately between 6 mm and 25 mm.

2. The collision skin depth of the generated plasma is expressed as follows:

$$\delta = \sqrt{\frac{2}{\mu_0 \omega \sigma_p}} \tag{2}$$

($\upsilon_m \gg \omega$, that is, the elastic collision frequency is higher than the electromagnetic wave frequency.) where $\mu_0$ is the permeability of vacuum, $\sigma_p$ is the plasma conductivity, and $\omega = 2\pi f$ is the angular frequency of the RF power. The formula indicates that the skin depth is determined by the plasma conductivity $\sigma_p$, which is mainly affected by the density of electrons, especially high-speed or high-temperature electrons, in the discharge chamber. The higher the plasma density and the conductivity $\sigma_p$ are, the lower the plasma resistance and the skin depth will be.

RF electromagnetic waves cannot easily penetrate the generated RF-ICP; therefore, to complete the ignition process efficiently and to increase the coupling efficiency in the E mode, the electromagnetic field induced in the skin depth must cover the entire discharge chamber. Moreover, when the skin depth is greater than the radius of the discharge chamber, the attenuated electromagnetic field exhibits a prominent peak in the axial center of the discharge chamber. The width of this peak is approximately half the width of the plasma, and this peak considerably enhances the skin depth effect and maximizes the effect of the induced electric field [36]. In the H mode, when $\delta$ is smaller than the radius of the discharge chamber, the generated plasma can absorb considerable power at the device edge [37].

## 2.5. E-H mode transition

During gas discharge in the RF band, the energy of the RF coil is coupled to the electrons in two modes: the capacitively coupled electrostatic mode (E mode) and inductively coupled electromagnetic mode

(H mode). During the working process of RF-ICP, discharge begins in the E mode, and low-density plasma is formed. E mode–H mode transitions occur when the plasma density increases to a specific value with an increase in the power coupled to the plasma. The critical plasma density for this conversion process is generally considered to be approximately $10^{16}\mathrm{m}^{-3}$–$10^{17}\mathrm{m}^{-3}$. These transitions result in a sudden increase in the electron density, which increases the ionization rate or dissociation rate considerably; thus, the discharge chamber pressure increases considerably. In particular, when the discharge gas is an electronegative gas, the E mode–H mode transitions become highly complex [38]. because of the instability and leakage effect during the discharge process of the electronegative gas. The Bohm velocity and the potential drop from the center of the generated plasma to its edge are smaller for electronegative plasma than for electropositive plasma [39]. In practical applications, RF-ICP can easily switch between the E and H modes, especially when a low power supply is required as the driving source and the plasma density remains stable.

The threshold current is not particularly clear during E mode–H mode transitions [40]. Therefore, we referred to Turner and Lieberman's calculations and discussions of the hysteresis behavior of the power parameter on the mode transition effect. The reactive gas is argon, and the starting current of the H mode at the 0-coordinate point originates from the E mode (represented by power). Fig. 5 indicates that when the electron density or power is high, the current in the coil sometimes does not increase with the power and might even decrease, which is similar to the experimental test results obtained in Ref. [41]. The dotted line in Fig. 5 [42] represents the change in absorbed power $P_{abs}$ of the coil current between the starting current and the H-mode sustain current, and the solid line represents the change of the dissipated power $P_{dis}$. The intersection of these two lines is the critical point for achieving stable H-mode operation. At the critical point, the electron density and ion density are approximately $6 \times 10^{16}$ $\mathrm{m}^{-3}$. The collision-free skin depth at this electron density is approximately 16 mm, and the skin depth decreases rapidly with the transition to the stable H mode to enable the generated RF-ICP to adapt to this mode stably. Moreover, under the back-leakage effect, the discharge process occurs in the E mode but still remains stable. At this time, the skin depth must span the radius of the discharge chamber. Considering that the skin depth is highly unstable because of the action of the internal current of the generated plasma, the radius of the discharge chamber is selected to be between 6 and 16 mm on the basis of the aforementioned discussion to ensure that the collision-free skin depth can penetrate the entire discharge chamber during E mode–H mode transitions.

### 2.6. Principle of kriging

Various surrogate models have been developed for reliability analysis. Mainstream surrogate models include the polynomial response surface, support vector machine, Kriging, and neural network models. The Kriging model includes a polynomial stochastic process function. To improve the accuracy of the reliability index obtained with this model, the following approaches have been proposed:

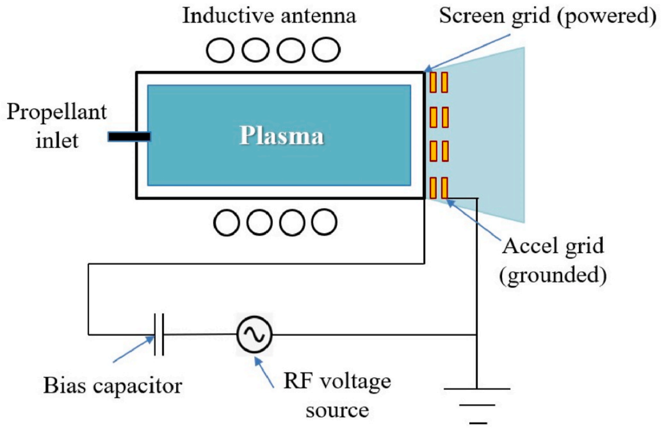

**Fig. 4.** Schematic of inductively coupled plasma.

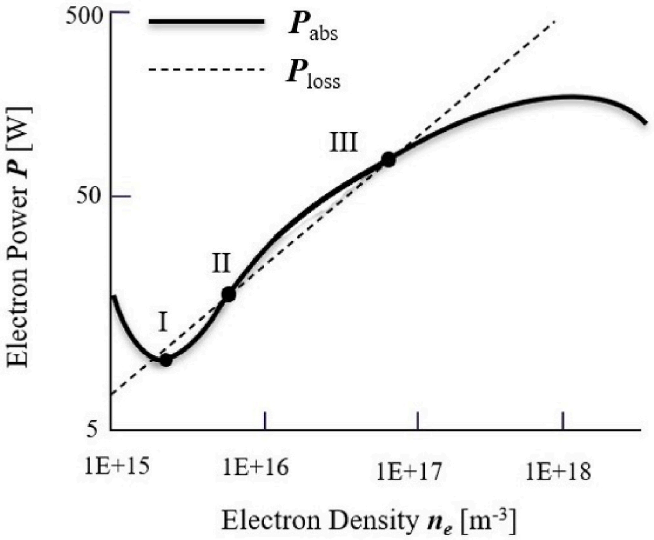

**Fig. 5.** Balance diagram of the electron density and power.

1. (1) Optimizing parameter $\theta$ of the Kriging model's correlation function.
2. (2) Identifying the best sample points through optimization, that is, selecting the best sample points through active learning and then refitting the Kriging model.
3. (3) Selecting different digital simulation methods, which involve generating sample points by constructing a candidate point set, to determine the structural failure probability.

In general, Latin hypercube sampling (LHS) and Monte Carlo sampling (MCS) are used to construct the initial point set, which becomes the initial design point. Different sampling methods, such as MCS, the subset simulation method, line sampling, and the Kriging method, are combined to calculate the structural reliability index [43].

The Kriging model comprises polynomial regression and random processes [44], which usually include the Gaussian process and exponential process. In this study, the Gaussian process was uniformly used for calculation. The Kriging model requires $k$ initial experiment points ($X = [x_1, x_2, \ldots, x_k]^T$ and the $i$th experiment $x_i \in R^n (i = 1, 2, \ldots, k)$. On the basis of correlation analysis, values are obtained for the $k$ experiment points ($Y = [Y(x_1), Y(x_2), \ldots, Y(x_k)]^T$). On the basis of the Kriging surrogate model, these values can be expressed as follows:

$$\widehat{Y} = F(\beta, x) + z(x) = f^T(x)\beta + z(x) \tag{3}$$

where x is an arbitrary input, $\widehat{Y}$ is the corresponding predicted response value, $\beta^T = [\beta_1, \beta_2, \ldots \beta_p]$ is a vector of the regression coefficients, and $f^T = [f_1(x), f_2(x), \ldots f_p(x)]$ is a vector of the polynomial basis function. Research has indicated that the specific forms of $F(\beta, x)$ do not considerably affect the fitting accuracy of the Kriging model. Hence, $\boldsymbol{f}^T(x)$ is considered the fixed coefficient vector $I$; thus, $F(\beta, x) = \beta$. Term z(x) represents a Gaussian random process that satisfies $N(0, \sigma^2)$. The covariance of the two arbitrary points $x_i$ and $x_j$ can be expressed as follows:

$$\mathrm{Cov}\left[Z(x_i), Z(x_j)\right] = \sigma^2 \, R(\theta, x_i, x_j) \tag{4}$$

where R($\theta$, $x$, $x'$) is the correlation matrix between $x$ and $x'$. This matrix can be expressed as follows:

$$R(\theta,x,x')\prod_{j=1}^{d}cor(\theta,x_i-x_j) \tag{5}$$

The Gaussian correlation function is defined as follows:

$$R(\theta,x_i,x_j)=exp\left(-\theta|x_i-x_j|^2\right),i=1,2,\dots j \tag{6}$$

The Gaussian correlation function adopted in this study is expressed as follows:

$$R(\theta,x_i,x_j)=exp\sum_{e=1}^{n}\left[-\theta_e\left(x_i^e-x_j^e\right)^2\right]\theta_e\geq 0 \tag{7}$$

where $x_i^e$ and $x_j^e$ represent the ***e***th direction component of the sample points $x_i$ and $x_j$, respectively, and $\theta_e$ is the correlation coefficient of the ***e***th direction component, demonstrating the relationship of the distance between design sample points with the correlation between these points. Parameter $\theta_e$ directly controls the predicted results of the Kriging model.

## 3. Experimental setup

### 3.1. Vacuum & pump system

Electric propulsion systems usually require a high-vacuum or ultrahigh-vacuum environment for ignition. Because the injection and discharge of propellant are inevitable in electric propulsion, the requirements for the pumping system are considerably different from those for static vacuum equipment. In addition, sometimes, the electric propulsion process has requirements related to not only the degree of vacuum but also the partial pressure of individual gasses in the vacuum environment. Therefore, close attention should be paid to the selective pumping characteristics of the vacuum pump when a vacuum pumping system is designed. In this study, we used a stainless-steel cylindrical vacuum chamber with a diameter of 50 cm and a length of 60 cm to conduct experiments (Fig. 6). Several flanges and quartz windows on the chamber served as feedthroughs and observation sites, respectively. The pump system comprised a dry pump (PTS06003 UNIV, Agilent Technologies Inc., Santa Clara, CA, United States), turbo molecular pump (HIPace 80, Pfeiffer Vacuum GmbH, Asslar, Germany), and water-cooling system [45–47,56]. The background pressure in the testing of the designed ion thruster was $10^{-5}$ to $10^{-3}$ torr to simulate the conditions associated with a Low-Earth orbit (LEO).

**Fig. 6.** Vacuum Chamber & Pump System used for experiments.

### 3.2. RF power system & RF coil

A coupled power supply is required to achieve ICP discharge. Typically, RF power is transmitted through an impedance matching network to the coil outside the discharge chamber and then coupled into the plasma. The RF power is coupled to the discharge chamber through a high-frequency oscillating coil, whose current induces a secondary electric field [48] that accelerates electrons, increases their collisions with the working medium (the propellant), and ionizes the propellant, which results in the generation of a plasma sustaining discharge. As displayed in Fig. 7, the circuit used for producing RF discharge usually contains parts such as an RF power generator, a matching box, several coaxial cables, and an RF coil. RF coaxial cables are required for transmission to reduce power loss because RF power sources are high-frequency current sources. The matching box (ADTEC AX-600, 600 W, 13.56 MHz, Japan) matches the input and output impedances. In the optimal matching condition, the incident power coupled into the plasma can reach a maximum value, and the corresponding reflected power is approximately 0. The RF source is powered by a DC power supply in the laboratory. To alleviate the external interference that affects the RF source, the matching network (which contains the RF source) is shielded for improving the matching performance.

To achieve the maximum RF power transmission efficiency, the load should be matched with the RF source to obtain the maximum undistorted power. We constructed a passive network between the end of the transmission line and the load, which is often called a matching network, to match the impedance in every discharge. When impedance matching is not achieved between the RF source and the load, the power transmission efficiency is quite low. Moreover, in severe cases, the transmission line and matching device might be damaged by heat [49]. For achieving maximum power transmission, the matching network's input impedance should be the conjugate of the source impedance, whereas the output impedance should be the conjugate of the load impedance. The characteristic impedance and length of the coaxial cable used in the conducted experiments were 50 Ω and 1 m, respectively [50]. Therefore, the cable's impedance requirements must be considered when calculating the RF source and load impedances.

### 3.3. Discharge chamber & gas distributor

During the discharge process, sputtering (i.e., ion erosion) occurs in the ionization chamber. Considering the secondary electron emission coefficient, the discharge chamber is often made of insulating and high temperature–resistant materials, such as quartz and alumina. To perform observations easily and avoid high costs, the material of the discharge chamber is selected to be acrylic. The chamber length is

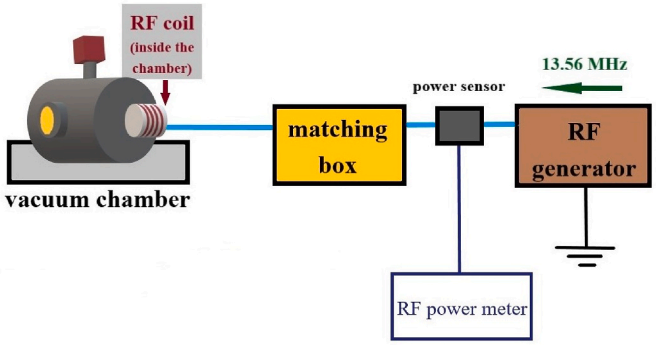

**Fig. 7.** Schematic of the RF power system.

selected on the basis of two considerations. First, an increase in the length of the ionization chamber increases the residence time of the propellant gas in the chamber, which considerably increases the propellant utilization rate and thruster efficiency. However, an excessive thruster length causes an increase in the thruster's surface-to-volume ratio, which leads to an increase in the avoidance loss of the plasma. Therefore, an optimal value exists for the aspect ratio of the thruster. By developing and testing different types of thrusters, the University of Gieβen summarized the relationships between the length of the ionization chamber, the discharge voltage, the discharge frequency, and the diameter of the ionization chamber. With the miniaturization of a RIT [40], the length of the thruster should be reduced, whereas the discharge voltage and frequency of the thruster should be increased.

The gas distributor affects the inlet mode and uniformity of the propellant, and a reasonable inlet mode can increase the residence time of the gas in the chamber [51]. A higher spatial uniformity increases the RF discharge, which enhances the propellant utilization rate of the thruster. The inlet aperture of the gas distributor is set as 8 mm, and 12 radial outlet holes with an aperture of 1 mm are evenly arranged at the bottom (Fig. 8). The uniform distribution of air outlet holes in the radial direction can cause argon gas to form a swirling flow, which increases the residence time in the ionization chamber and the utilization rate of the working medium. Length *d* of the gas distributor intruding into the discharge chamber is 8 mm.

### 3.4. *Ion optics & neutralizer*

The grid system is the power source and ion extraction and acceleration device of the thruster [42]. When the ions generated through ionization in the discharge chamber are close to the screen grid, they are extracted under the Child–Langmuir sheath and accelerated by the bias voltage applied between the grids to generate thrust [43]. Therefore, the grid is critical to the operation of the ion thruster, and its performance, life, size, and other factors must be considered in its design. Many factors influence the design of an ion thruster grid. The screen grid extracts ions from the plasma, and these ions are then focused by a downstream accelerating grid. The ion current drawn by the grid varies with the power and thrust requirements; therefore, ion focusing must be conducted under different ion densities to ensure a high thruster efficiency. Because the screen grid is in direct contact with the discharge chamber, the transparency of the screen grid directly affects the ion extraction rate. The grid system must minimize the bombardment of the grid by ions. Moreover, the ions reaching the gate surface are extracted from the plasma region, and the escape of the propellant gas from the ionization chamber should be minimized to increase the propellant utilization rate. In summary, a high ionic transparency and low gas atomic transparency are required. To achieve these requirements, the screen grid must have a large aperture, whereas the acceleration grid must have a small aperture.

## 4. Thruster performance

### 4.1. *Plasma diagnostics*

The final design of the thruster is presented in Fig. 9. The most common tool used for plasma-related measurements is the Langmuir probe, which is a long metal stick that is usually made of molybdenum or tungsten. We inserted this probe inside the discharge chamber of the designed ion thruster to measure the plasma density and electron temperature, and an oscilloscope plotted the IV curve. However, because of the potential fluctuations of the generated ICP, the plotted IV curve was distorted by the RF signal, which led to the generation of probe noise. Because a customized RF compensated Langmuir probe was unavailable, we measured the ion beam current, which can be easily detected by a copper plate (by using the Faraday cup method) with a distance of four times the chamber's diameter (Fig. 10) in accordance with the Child–Langmuir law [52].

### 4.2. *Estimation of performance*

To create a database for the Kriging model, three parameters (the propellant flow rate, the voltage difference between the grids, and the RF input power) are selected and the ion beam current is chosen to be the metric/index in Table 2. The equations that we utilize are listed in Table 3. Then, we list the thruster performance in Table 4 with the Latin Hypercube Sampling (LHS) method. The finest combination of the three parameters (Case no. 18 in the selected 30 cases) is 4 sccm of the propellant flow rate, 3000 V of the grid voltage difference, and 40 W of the RF input power, yielding the results: 38.4 mA of beam current, 1.92 mN of thrust, 1649.55 s of specific impulse, 16165.65 m/s of exhaust velocity, and 33.7% of mass utilization efficiency.

## 5. Thruster optimization

### 5.1. *Prediction from kriging model*

Visualized Kriging models (Fig. 11) were produced using the values of the parameters listed in Table 2 through the MATLAB software program. In the analysis of the Kriging models, coefficients of $10^{-0.715}$, $10^{-0.096}$, and $10^{1.255}$ were obtained for the propellant flow rate, grid voltage difference, and RF input power, respectively. These coefficients represent the influences of the corresponding parameters on the polynomial generated by the Kriging models, with the absolute values of the coefficients representing the influence magnitudes of the corresponding

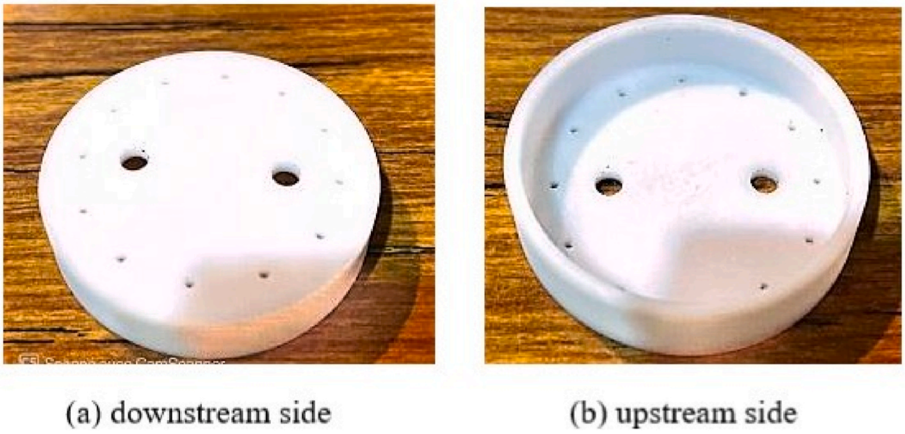
(a) downstream side (b) upstream side

**Fig. 8.** Gas Distributor with two ostiums for the Ignitor wires.

parameters. In this study, the RF input power had the strongest effect on the generated polynomial, followed by the grid voltage difference and propellant flow rate.

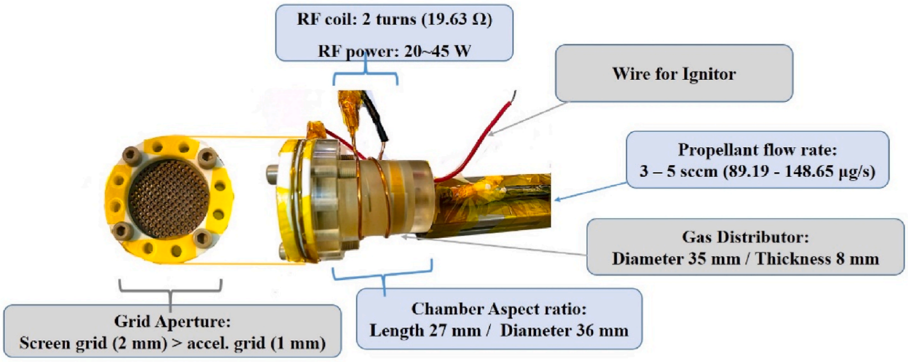

**Fig. 9.** Design of the RF Ion Thruster in this study.

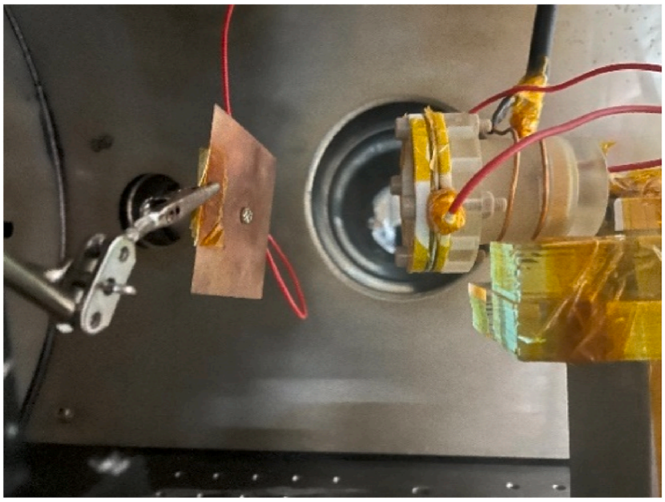

**Fig. 10.** Measurement of ion beam current.

**Table 2**
Determination of Parameters and their Ranges.

| Design variables | | Constraints |
|---|---|---|
| $m'$ | Propellant mass flow rate [sccm] | 3–5 |
| $V_b$ | Grids voltage difference [V] | 500–2500 |
| $P_{RF}$ | RF input power [W] | 20–45 |
| Objective functions | | Definitions |
| $I_b$ | Ion beam current [mA] | Current formed by the accelerated ions |
| $T$ | Thrust [mN] | $\mathrm{T} = \sqrt{\frac{2M}{q}} \times I_b\sqrt{V_b} = 913.285 \times I_b\sqrt{V_b}$ |

**Table 3**
Estimated metrics with the calculation of ion beam current.

| Metrics | Equation |
|---|---|
| Thrust (mN) | $T = \sqrt{\frac{2M}{q}} \cdot I_b\sqrt{V_b} = 913.285 \cdot I_b\sqrt{V_b}$ |
| Specific Impulse ($I_{\mathrm{sp}}$) | $I_{sp} = \frac{T}{m'g}$ |
| Exhaust velocity (m/s) | $v_i = \sqrt{2\frac{q}{M}(V_{exit} - V_{inlet})} = \sqrt{\frac{2qV_b}{M}} = \frac{T}{m'}$ |
| Mass utilization rate (%) | $\frac{I_b \bullet M_i}{e \bullet m'} = \frac{I_b \bullet 1.67 \times 10^{-27}}{1.6 \times 10^{-19} \bullet m_i'}$ |

### 5.2. *Interpretation of kriging model*

The following findings were obtained from the generated Kriging models.

(1) In the designed RIT, the beam current is not exactly proportional to the propellant flow rate. This finding is in agreement with the ion energy distribution curves displayed in Ref. [53]. The beam current initially increases with the propellant flow rate. However, at a certain propellant flow rate, the beam current no longer increases with this rate because of the increasing ratio taken by the neutral gas. Moreover, the recombination rate increases, which causes a decrease in the ion flux density.

(2) On the basis of the equation of the ion beam current ($I_{b_{max}} = \frac{4\varepsilon_0}{9}\sqrt{\frac{2q}{M_i}} \bullet \frac{V_b^{\frac{3}{2}}}{l_e} \bullet A_s \bullet \varphi_s$) and the RF-ICP mechanism, the grid voltage difference was discovered to be positively correlated with the RF input power. Among the considered parameters, the RF input power has the strongest effect on the ion beam current because the RF input power provides the coupling power to the generated ICP.

However, the ion beam current does not necessarily increase with RF power; two explanations are possible:

(i) The RF power is used for ionizing the neutral gas (the propellant) and heating the generated plasma. When the electron temperature reaches a specific level, a considerable portion of the RF power is used for plasma heating instead of ionization.

(ii) Kriging model may need more database than used 30 cases (see Table 4).

In the present study, on the basis of the scaling law proposed by the University of Gieβen, an acrylic discharge chamber with a diameter of 36 mm and a length of 27 mm is designed to upgrade the ion thruster developed in the previous study (Table 5) [54,55].

## 6. Conclusions

The experiments conducted in this study indicate the importance of the parameters related to the discharge chamber, RF coil, and grid system for the RIT. Initially, because of the lack of knowledge regarding a suitable inner pressure, the designed chamber failed to ignite irrespective of the increase in the propellant flow rate. After considerable trial and error, it was discovered that the best solution is to install a gas distributor in the designed system. Moreover, the impedance matching problem was solved by using an impedance analyzer and a matching box. The effects of three parameters, namely the propellant flow rate, grid voltage difference, and RF input power are analyzed on the results

**Table 4**
Performance of the RF Ion Thruster in this study.

| Case | | | | Index | Estimated Performance | | | |
|---|---|---|---|---|---|---|---|---|
| No. | Flow rate (sccm) | Voltage Difference (V) | RF Input Power (W) | Ion beam Current (mA) | Thrust (mN) | $I_{sp}$ (s) | Exhaust velocity (m/s) | Mass utilization efficiency (%) |
| 1 | 4.5 | 500 | 25 | 0.87 | 0.02 | 19 | 187 | 0.6 |
| 2 | 3.5 | 1000 | 25 | 2.37 | 0.08 | 82 | 806 | 2.3 |
| 3 | 3.0 | 500 | 35 | 1.61 | 0.04 | 53 | 521 | 1.8 |
| 4 | 4.0 | 1000 | 30 | 8.11 | 0.28 | 246 | 2413 | 7.1 |
| 5 | 3.5 | 2500 | 35 | 22.79 | 1.14 | 1118 | 10961 | 22.8 |
| 6 | 5.0 | 2000 | 30 | 17.77 | 0.81 | 557 | 5461 | 12.4 |
| 7 | 3.5 | 1500 | 20 | 0.82 | 0.03 | 32 | 322 | 0.8 |
| 8 | 5.0 | 2500 | 25 | 13.54 | 0.67 | 465 | 4558 | 9.5 |
| 9 | 4.0 | 2000 | 40 | 2.80 | 0.12 | 109 | 1075 | 2.4 |
| 10 | 4.0 | 500 | 30 | 14.54 | 0.42 | 360 | 3533 | 12.7 |
| 11 | 3.5 | 1000 | 40 | 2.80 | 0.09 | 97 | 952 | 2.8 |
| 12 | 3.0 | 2500 | 45 | 31.44 | 1.57 | 1800 | 17642 | 36.7 |
| 13 | 5.0 | 1000 | 35 | 26.99 | 0.95 | 655 | 6425 | 18.9 |
| 14 | 4.5 | 1000 | 20 | 0.83 | 0.02 | 22 | 219 | 0.64 |
| 15 | 4.5 | 1500 | 25 | 3.10 | 0.12 | 96 | 946 | 2.4 |
| 16 | 5.0 | 1500 | 40 | 17.82 | 0.72 | 499 | 4898 | 12.5 |
| 17 | 5.0 | 2000 | 45 | 35.66 | 1.62 | 1118 | 10960 | 25.0 |
| 18 | 4.0 | 2500 | 40 | 38.41 | 1.92 | 1649 | 16165 | 33.7 |
| 19 | 4.0 | 1500 | 35 | 29.99 | 1.22 | 1051 | 10305 | 26.3 |
| 20 | 3.0 | 2000 | 20 | 0.86 | 0.03 | 44 | 440 | 1.0 |
| 21 | 4.5 | 1500 | 20 | 0.87 | 0.03 | 27 | 265 | 0.6 |
| 22 | 3.0 | 1000 | 45 | 22.44 | 0.79 | 908 | 8904 | 26.2 |
| 23 | 3.0 | 500 | 40 | 7.02 | 0.20 | 232 | 2274 | 8.2 |
| 24 | 4.0 | 2000 | 30 | 5.47 | 0.24 | 214 | 2101 | 4.8 |
| 25 | 4.5 | 2000 | 40 | 22.32 | 1.01 | 777 | 7622 | 17.4 |
| 26 | 4.0 | 1500 | 30 | 9.27 | 0.37 | 325 | 3185 | 8.1 |
| 27 | 3.5 | 1500 | 25 | 1.15 | 0.04 | 46 | 451 | 1.1 |
| 28 | 4.5 | 1000 | 40 | 6.12 | 0.21 | 165 | 1618 | 4.7 |
| 29 | 3.5 | 1000 | 30 | 12.27 | 0.43 | 425 | 4173 | 12.3 |
| 30 | 4.0 | 2500 | 25 | 4.00 | 0.97 | 171 | 1683 | 3.5 |

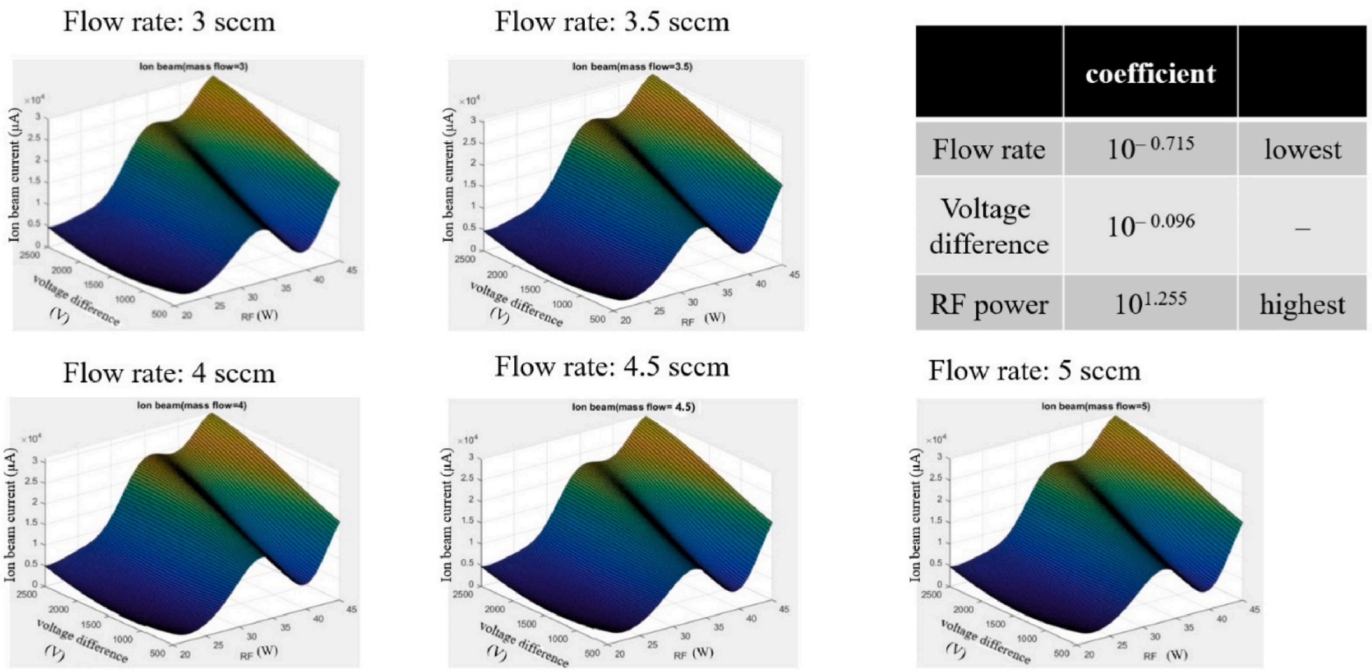

| | coefficient | |
|---|---|---|
| Flow rate | $10^{-0.715}$ | lowest |
| Voltage difference | $10^{-0.096}$ | – |
| RF power | $10^{1.255}$ | highest |

**Fig. 11.** Plots of the Kriging model with the flow rate from 3 sccm to 5 sccm.

of the Kriging model. On the basis of the results obtained with the Kriging model, the following findings were obtained:

(1) The failure of plasma ignition can be overcome by increasing the inner pressure, propellant flow rate, gas distributor, and most importantly, the RF input power.

(2) The ion beam current and thrust can be enhanced by increasing the propellant flow rate, grid voltage difference, and RF input power. However, the specific impulse and thruster efficiency should be considered when the grid voltage difference and RF input power are increased.

**Table 5**
Improvement of the Previous study.

| Item | ZAPLab [54,55] | This research |
|---|---|---|
| gas feeding system | only gas inlet | additional gas distributor |
| Argon flow rate | 17–32 sccm | 3–5 sccm |
| background pressure | $2 \times 10^{-3}$ torr | $8.1 \times 10^{-4}$ torr |
| discharge chamber aspect ratio | $\frac{70}{38}$ | $\frac{18}{36} \sim \frac{27}{36}$ |
| RF power system | handmade | off-the-shelf equipment |
| RF coil turns | 85 turns | 2–3 turns |
| grid aperture | screen < accel.<br>poor transparency | screen > accel.<br>based on the effective acceleration length $l$ (Section 3.4) |

(3) The material of the discharge chamber should be altered to quartz glass or ceramic alumina to achieve higher heat resistance. Moreover, the grid system can be redesigned on the basis of the results of Kriging model–based experiments.

## Declaration of competing interest

The authors declare that they have no known competing financial interests or personal relationships that could have appeared to influence the work reported in this paper.

## Acknowledgments

Financial support for this work was provided by the Ministry of Science and Technology (Taiwan) under grant numbers MOST 108-2628-E-006- 008-MY3, MOST 110-2622-E-006-029, and provided by National Science and Technology Council (Taiwan) under grant number NSTC 111-2224-E-006-008.

## References

[1] A. Lopez Ortega, B. Jorns, I.G. Mikellides, R.R. Hofer, Numerical simulations of the XR-5 Hall thruster for life assessment at different operating conditions, in: 51st AIAA/SAE/ASEE Joint Propulsion, 2015, p. 4008.

[2] J.S. Snyder, G. Lenguito, J.D. Frieman, T.W. Haag, J.A. Mackey, Effects of background pressure on SPT-140 Hall thruster performance, J. Propul. Power 36 (2020) 668–676.

[3] O. Duchemin, J. Rabin, L. Balika, G. Coduti, V. Vial, D. Vuglec, et al., Qualification status of the PPS® 5000 Hall thruster unit, in: Proceedings of the 36th International Electric Propulsion Conference: IEPC-2019-906, University of Vienna Austria, 2019.

[4] W. Tighe, K.-R. Chien, E. Solis, P. Rebello, D. Goebel, J. Snyder, Performance evaluation of the XIPS 25-cm thruster for application to NASA discovery missions, in: AIAA/ASME/SAE/ASEE Joint Propulsion Conference & Exhibit, 42nd, 2006, p. 4666.

[5] M. Hutchins, H. Simpson, J.P. Jiménez, QinetiQ's T6 and T5 ion thruster electric propulsion system architectures and performances, in: Joint Conference of 30th International Symposium on Space Technology and Science, 34th International Electric Propulsion Conference, and 6th Nano-Satellite Symposium, 2015.

[6] R. Killinger, H. Bassner, H. Leiter, R. Kukies, RITA Ion Propulsion for Artemis. 37th Joint Propulsion Conf, 2001.

[7] H.W. Löb, K.-H. Schartner, B.K. Meyer, D. Feili, St KD. Weis, Forty years of Giessen EP-activities and the recent RIT-microthruster development, in: International Electric Propulsion Conference, 29 th, Princeton University, Princeton, USA, 2005.

[8] K. Holste, W. Gärtner, D. Zschätzsch, S. Scharmann, P. Köhler, P. Dietz, et al., Performance of an iodine-fueled radio-frequency ion-thruster, Eur. Phy. J. D 72 (2018) 1–7.

[9] C.M. Collingwood, S.B. Gabriel, M.H. Corbett, P. Jameson, The MiDGIT thruster: development of a multi-mode thruster, in: 31st International Electric Propulsion Conference, Michigan, Ann Arbor, 2009.

[10] N. Antropov, R. Akhmetzhanov, A. Bogatyy, R. Grishin, V. Kozhevnikov, A. Plokhikh, et al., Experimental research of radio-frequency ion thruster, Therm. Eng. 63 (2016) 957–963.

[11] V. Mistoco, S. Bilén, M. Micci, Development and chamber testing of a miniature radio-frequency ion thruster for microspacecraft, in: AIAA/ASME/SAE/ASEE Joint Propulsion Conference and Exhibit, 40th, 2004, p. 4124.

[12] M. Tsay, J. Model, C. Barcroft, J. Frongillo, J. Zwahlen, C. Feng, Integrated Testing of Iodine Bit-3 Rf Ion Propulsion System for 6u Cubesat Applications, 35th International Electric Propulsion Conference, Atlanta, USA, 2017.

[13] M. Tsay, K. Hohman, N. Rosenblad, E. Ehrbar, M. Robin, C. Farnell, Micro radio-frequency ion propulsion system, in: 48th AIAA/ASME/SAE/ASEE Joint Propulsion Conference & Exhibit, 2012, p. 3947.

[14] T.A. Trudel, S.G. Bilén, M.M. Micci, Design and Performance Testing of a 1-cm Miniature Radio-Frequency Ion Thruster. 31st Internationational Electric Propulsion Conference, 2009, pp. 20–24. IEPC.

[15] J.M. Martinez, D. Rafalskyi, A. Aanesland, Development and Testing of the NPT30-I2 Iodine Ion Thruster, 36th International electric propulsion conference, 2019.

[16] I. Borodin, M. Silnikov, K. Kulakov, Numerical calculation of the operating parameters of the ION engine for satellite correction, Acta Astronaut. (2022).

[17] M. Silnikov, K. Kulakov, S. Kulakov, D. Panov, Correction thruster development based on high-current surface discharge in vacuum, Acta Astronaut. 109 (2015) 177–181.

[18] A. Alexandrov, E. Kralkina, V. Pavlov, A. Rukhadze, A. Bugrova, G. Bugrov, et al., On the Possibilities of RF Ion Thrusters Optimization, 29th Intern Electric Propulsion Conf(IEPCO5), Princeton, NJ, 2005. October 31±November.

[19] K. Hiramoto, Y. Takao, Investigation of ion beam extraction mechanism for higher thrust density of ion thrusters, Trans. Jpn. Soc. Aeronaut. Space Sci. Aerospace Technol. Jpn 14 (2016) Pb_57–Pb_62.

[20] E. Kralkina, K. Vavilin, I. Zadiriev, P. Nekliudova, G. Shvydkiy, Optimization of discharge parameters in an inductive RF ion thruster prototype, Vacuum 167 (2019) 136–144.

[21] N. Yan, N. Guo, C. Wu, Z. Gu, Z. Yang, Research on RF-ion thruster based on discharge chamber uniform model, Chin. Space Sci. Technol. 41 (2021) 1.

[22] P. Chabert, J. Arancibia Monreal, J. Bredin, L. Popelier, A. Aanesland, Global model of a gridded-ion thruster powered by a radiofrequency inductive coil, Phys. Plasmas 19 (2012), 073512.

[23] A. Reeh, U. Probst, P.J. Klar, Global model of a radio-frequency ion thruster based on a holistic treatment of electron and ion density profiles, Eur. Phy. J. D 73 (2019) 1–21.

[24] P. Grondein, T. Lafleur, P. Chabert, A. Aanesland, Global model of an iodine gridded plasma thruster, Phys. Plasmas 23 (2016), 033514.

[25] B. Magaldi, J. Karnopp, A. da Silva Sobrinho, R. Pessoa, A global model study of plasma chemistry and propulsion parameters of a gridded ion thruster using argon as propellant, Plasma 5 (2022) 324–340.

[26] W. Jiang, L. Wei, X. Yang, Z. Yang, Influence of coil structure and position on the performance of miniature radio frequency ion thrusters, Vacuum (2023), 111911.

[27] Y. Yamashita, R. Tsukizaki, K. Nishiyama, Importance of stepwise ionization from the metastable state in electron cyclotron resonance ion thrusters, J. Electric Propulsion 1 (2022) 1–20.

[28] C. Maolin, S. Anbang, C. Chong, X. Guangqing, Particle simulation of grid system for krypton ion thrusters, Chin. J. Aeronaut. 31 (2018) 719–726.

[29] Y. Tani, Y. Yamashita, R. Tsukizaki, K. Nishiyama, H. Kuninaka, Effect of discharge chamber geometry on ion loss in microwave discharge ion thruster, Acta Astronaut. 176 (2020) 77–88.

[30] T. Roppel, D. Reinhard, J. Asmussen, Low temperature oxidation of silicon using a microwave plasma disk source, J. Vac. Sci. Technol. B 4 (1986) 295–298.

[31] T. Kitajima, Y. Takeo, Z.L. Petrović, T. Makabe, Functional separation of biasing and sustaining voltages in two-frequency capacitively coupled plasma, Appl. Phys. Lett. 77 (2000) 489–491.

[32] H.U. Eckert, Induction plasmas at low frequencies, AIAA J. 9 (1971) 1452–1456.

[33] E. Infeld, Basic principles of plasma physics: a statistical approach. By S. Ichimaru. Benjamin frontiers in physics, 1973. 324, J. Plasma Phys. 13 (1975) 571–572, 12.50 (paperback).

[34] B. Walsh, A. Stokes, Energy balance and stability of an induction heated plasma, Chem. Eng. Sci. 27 (1972) 511–518.

[35] J. Hopwood, Review of inductively coupled plasmas for plasma processing, Plasma Sources Sci. Technol. 1 (1992) 109.

[36] A. Howling, L. Sansonnens, J. Ballutaud, C. Hollenstein, J. Schmitt, Nonuniform radio-frequency plasma potential due to edge asymmetry in large-area radio-frequency reactors, J. Appl. Phys. 96 (2004) 5429–5440.

[37] G.A. Hebner, E.V. Barnat, P.A. Miller, A.M. Paterson, J.P. Holland, Frequency dependent plasma characteristics in a capacitively coupled 300 mm wafer plasma processing chamber, Plasma Sources Sci. Technol. 15 (2006) 879.

[38] P. Chabert, A. Lichtenberg, M. Lieberman, A. Marakhtanov, Instabilities in low-pressure electronegative inductive discharges, Plasma Sources Sci. Technol. 10 (2001) 478.

[39] P. Chabert, A. Lichtenberg, M. Lieberman, A. Marakhtanov, Dynamics of steady and unsteady operation of inductive discharges with attaching gases, J. Appl. Phys. 94 (2003) 831–843.

[40] U. Kortshagen, N. Gibson, J. Lawler, On the E-H mode transition in RF inductive discharges, J. Phys. Appl. Phys. 29 (1996) 1224.

[41] V. Godyak, R. Piejak, B. Alexandrovich, Experimental setup and electrical characteristics of an inductively coupled plasma, J. Appl. Phys. 85 (1999) 703–712.

[42] K.K. Jayapalan, O.-H. Chin, The effects of neutral gas heating on H mode transition and maintenance currents in a 13.56 MHz planar coil inductively coupled plasma reactor, Phys. Plasmas 19 (2012), 093501.

[43] M. Balesdent, J. Morio, J. Marzat, Kriging-based adaptive importance sampling algorithms for rare event estimation, Struct. Saf. 44 (2013) 1–10.

[44] I. Kaymaz, Application of kriging method to structural reliability problems, Struct. Saf. 27 (2005) 133–151.

[45] Y.-H. Li, K. Dorn, H.-C. Hsieh, T.-C. Kuo, Y.-C. Hsu, Effect of electode angle on pulsed plasma thruster performance, J. Aeronaut. Astronaut. Aviat. 53 (3) (2021) 353–368.

[46] Y.-H. Li, S. Palagiri, P.-Y. Chang, C. Montag, G. Heridrich, Plasma behavior in a solid-fed pulsed plasma thruster, J. Aeronaut. Astronaut. Aviat. 51 (1) (2019) 31–42.

[47] Y.-H. Li, J.-Y. Pan, G. Herdrich, Design and demonstration of micro-scale vacuum cathode arc thruster with inductive energy storage circuit, Acta Astronaut. 172 (2020) 33–46.

[48] D. Shaw, M. Watanabe, H. Uchiyama, G. Collins, Secondary electron energy spectra emitted from radio frequency biased plasma electrodes, Appl. Phys. Lett. 75 (1999) 34–36.

[49] J.-S. Nam, M.-Y. Lee, J.-H. Seo, G.-H. Kim, Numerical analysis on the electrical and thermal flow characteristics of Ar-$N_2$ inductively coupled plasma torch system, J. Kor. Phys. Soc. 72 (2018) 755–764.

[50] Y. Zhou, X. Xie, X. Zhang, K. Huang, Design and simulation of high-power RF power supply for ICP based on Simulink, in: IEEE 3rd International Conference on Electronic Information and Communication Technology (ICEICT), IEEE, 2020, pp. 291–294, 2020.

[51] Y. Nakayama, K. Narisawa, Neutral density measurement of ion thruster with differential pressure gauge, Trans. Jpn. Soc. Aeronaut. Space Sci. Aerospace Technol. Jpn. 12 (2014) Pb_73. Pb_8.

[52] D.L. Brown, M.L.R. Walker, J. Szabo, W. Huang, J.E. Foster, Recommended practice for use of Faraday probes in electric propulsion testing, J. Propul. Power 33 (2017) 582–613.

[53] X. Hai-long, J. Wei, L. Chuan-hui, D. Bo, R. Yong, M. Xin-chun, et al., Studies on the ion energy distribution of radio-frequency discharges, Nucl. Fusion Plasma Phys. 41 (2021) 598.

[54] T.-Y. Huang, Y.-H. Li, M.-H. Shen, Y.-C. Chen, Development of a miniature radio-frequency ion engine with inductively coupled plasma (ICP) source for cube satellite propulsion, AIAA Propulsion and Energy (2021 Forum).

[55] Y.-H. Li, T.-Y. Huang, M.-H. Shen, Y.-C. Chen, Development of miniature radio frequency ion thruster with inductively coupled plasma source, J. Aeronaut. Astronaut. Aviat. 55 (1) (2023) 13.

[56] B.-H. Huang, Y.-H. Li, H.-Y. Lee, J.H. Hsieh, Development of a new concept vacuum arc thruster with multilayer electrodes, AIAA Propulsion and Energy (2021 Forum) (2021).